HHS Public Access

Author manuscript

Nat Nanotechnol. Author manuscript; available in PMC 2024 August 18.

Published in final edited form as:

Nat Nanotechnol. 2024 August ; 19(8): 1158–1167. doi:10.1038/s41565-024-01658-6.

Phase-separated porous nanocomposite with ultralow percolation threshold for wireless bioelectronics

Yadong Xu[1,2,†], **Zhilu Ye**[3,†], **Ganggang Zhao**[4,†], **Qihui Fei**[1], **Zehua Chen**[1], **Jiahong Li**[2], **Minye Yang**[3], **Yichong Ren**[3], **Benton Berigan**[1], **Yun Ling**[4], **Xiaoyan Qian**[1], **Lin Shi**[1], **Ilker Ozden**[1], **Jingwei Xie**[5], **Wei Gao**[2,*], **Pai-Yen Chen**[3,*], **Zheng Yan**[1,4,6,7,*]

[1]Department of Chemical and Biomedical Engineering, University of Missouri, Columbia, MO 65201, USA

[2]Andrew and Peggy Cherng Department of Medical Engineering, Division of Engineering and Applied Science, California Institute of Technology, Pasadena, CA 91125, USA

[3]Department of Electrical and Computer Engineering, University of Illinois at Chicago, Chicago, IL 60607, USA

[4]Department of Mechanical & Aerospace Engineering, University of Missouri, Columbia, MO 65201, USA

[5]Department of Surgery-Transplant and Mary and Dick Holland Regenerative Medicine Program, University of Nebraska Medical Center, Omaha, NE 68130, USA

[6]Materials Science and Engineering Institute, University of Missouri, Columbia, MO 65201, USA

[7]NextGen Precision Health, University of Missouri, Columbia, MO 65211, USA

Abstract

Realizing the full potential of stretchable bioelectronics in wearables, biomedical implants and soft robotics necessitates conductive elastic composites that are intrinsically soft, highly conductive, and strain resilient. However, existing composites usually compromise electrical durability and performance owing to disrupted conductive paths under strain and rely heavily on high conductive filler content. Here we present an in-situ phase separation method that facilitates microscale silver nanowire assembly and create self-organized percolation networks on pore surfaces. The resultant nanocomposites are highly conductive, strain-insensitive, fatigue-tolerant, while minimizing filler usage. Their resilience is rooted in multiscale porous polymer matrices that dissipate stress and rigid conductive fillers adapting to strain-induced geometry changes. Notably, the presence of porous microstructures reduces the percolation threshold (V_c=0.00062) by 48-fold and suppresses electrical degradation even under strains exceeding 600%. Theoretical

*Corresponding author. yanzheng@missouri.edu, pychen@uic.edu, weigao@caltech.edu.
†These authors contribute equally to this work.

Author Contributions

Z. Y., Y. X., P. C., Zhilu. Y. conceived the idea and led research efforts. Y. X., Zhilu. Y., G. Z., Q. F., Z. C., J. L., M. Y., Y. R., Y. L., X.Q., L.S. and J.X. performed the experiments. J. L. conducted numerical simulations. I. O., and B. B. led animal studies and performed surgeries. Z.Y., Y. X., Zhilu. Y., and W. G. wrote the manuscript with assistance of other co-authors. Y. X., Zhilu. Y., and G. Z. contribute equally to this work.

Competing Interests

The authors declare no competing interests.

calculations yield quantitatively consistent results with experimental findings. By pairing with near-field communication technologies, we have demonstrated stretchable wireless power and data transmission solutions that are ideal for both skin-interfaced and implanted bioelectronics. The systems enable battery-free wireless powering and sensing of a breadth of sweat biomarkers—with less than 10% performance variation even at 50% strain. Ultimately, our strategy offers expansive material options for diverse applications.

Soft elastic conductive composite materials that exhibit high electrical conductivity[1,2], strain-insensitive performance[3–5], and skin-like mechanical compliance[6–9] are essential for next-generation soft robotics, skin-mounted and implanted devices[10,11]. They are pivotal in biomedical diagnostics, electronic skins, and human-machine interfaces[12–15]. System-level bioelectronic devices, composed of soft sensors and rigid electronic components[10,16], demand breathable sensors and strain-resilient conductors that offer exceptional mechanical tolerance. Present enabling technologies utilize conductive fillers dispersed in elastomer matrices, spanning from nanoparticles, nanowires/nanotubes, to nanosheets[12,13]. While liquid metal-based composites established a viable solution, their susceptibility to leakage, necessity of high loadings, and inevitable interface corrosion of electronic components over prolonged exposure pose challenges[17,18].

Given percolation theory, metal nanowires with high aspect ratio are preferred over other fillers to achieve highly conductive composites because they considerably reduce the percolation threshold[12]. Recent endeavors span from the fabrication of silver nanowires (Ag NWs) nanocomposites with notable electrical conductivity to ultrathin nanomembrane with facile patternability[1,2]. Nonetheless, persistent challenges remain, including the pronounced electromechanical coupling, rapid degradation in cyclic fatigue test, tedious ligand exchange process, and the necessity for substantial filler loadings (60-80% by weight). Minimizing filler usage is essential to achieve cost-effectiveness, reduce macroscopic stiffness, and enhance stretchability. Additionally, macroscale stretching of nanocomposites generally results in diminished overlap of percolation pathways, thereby compromising their electrical performance. Strain-induced self-organization and rearrangement of the conductive fillers within the polymer represents a promising strategy[19–21], yet the synthesis and separation of fillers from the polymer at microscale level are fundamentally challenging.

Porous elastomer conductors, characterized by high breathability, ultra-softness, and large surface area, can find broad applications[9,22–24]. Various techniques, including hard-templating, freeze-drying, emulsion, breath figure methods, and electrospinning, have been employed to introduce porous structures[9,24,25]. Specifically, porous Ag NWs elastomer composites with notable breathability has been achieved[26,27]. However, these methods often yield materials with significant electrical-mechanical coupling. Besides, phase-separation have gained considerable attention for creating interconnected and tunable porous polymer structures in a simple, cost-effective, and template-free manner[28,29]. Representative applications include thermal management, sensing, catalysis, energy storage, and water purification[23,28,30]. Furthermore, phase separation has been applied to produce porous conductors by embedding conductive fillers within polymer matrices. However, these materials usually lack strain-insensitive property[23,31].

Here, we report a one-step, in situ phase separation of Ag NWs from porous polyurethane (PU) matrices (Fig. 1a). This process facilitates microscale assembly of Ag NWs, forming self-organized percolation networks on pore surfaces. Consequently, we achieve an electrically conductive phase-separated porous Ag NWs nanocomposite (PSPN) with extremely low percolation threshold and strain-insensitive electrical property. The latter arises from the synergy of energy-dissipative porous PU microstructures and adaptable Ag NWs conductive pathways, maintaining effective electron transport even under significant macroscopic strain (Fig. 1b, c). We demonstrate simultaneous accomplishment of electrical-mechanical decoupling, ultralow percolation thresholds, and remarkable electrical conductivity despite the low Ag NWs volume fractions. This strategy also eliminates the ligand-exchange process typically required for Ag NWs-based composites. Leveraging these unique attributes, we pair our PSPN with near field communication (NFC)-based technologies to achieve wireless power delivery and data transmission for skin-interfaced and implantable bioelectronic devices.

Phase separation and theoretical prediction

The fabrication of PSPN begins with the preparation of a precursor solution containing polymer solution (PU in tetrahydrofuran, THF) and conductive filler solution (Ag NWs in ethanol). During the subsequent drop-casting process, phase separation initiates due to the evaporation of the volatile solvent (THF) and nonsolvent (ethanol). This results in the separation of the PU-rich and PU-poor phase. Ag NWs with amphiphilic ligands (i.e., polyvinyl pyrrolidone) reside in the PU-poor phase due to its immiscibility with PU solution. The liquid-liquid demixing process generates co-continuous phases in three dimensions, completed by coarsening that creates continuous porous structures within the PU matrices. Fig. 1a presents a 2D cross-sectional view of the phase separation process, whereas Supplementary Fig. 1 provides a complementary 3D schematic of the PSPN. This process can be elucidated by examining the trajectory of the compositional path of the nanocomposite solution within the phase diagram (Fig. 1d)[28,29,32,33]. The pore sizes are tunable by changing the nonsolvent content (Supplementary Fig. 2). Throughout this process, Ag NWs initially self-organize closely on the pore surfaces, gradually forming strain-adaptive percolation networks as characterized by an increasing number of nanowires. As illustrated in Supplementary Fig. 3, the natural evaporation of THF and ethanol is essential for the formation of porous nanocomposites. The microscopic-level self-assembly of Ag NWs, guided by the presence of micro-sized pores, is driven by minimizing the free energy to stabilize the system (i.e., Pickering effect)[34].

Conductive nanocomposites are generally made by uniformly dispersing conductive filler materials within soft elastomer matrices, where these nanomaterials establish conductive percolation networks (i.e., multiple continuous electron transport paths) once a critical density is reached[12]. For example, strain-induced rupture of Ag NWs percolation networks typically occurs upon macroscopic stretching[19] (Fig. 1c). In the presence of an energy dissipative porous microstructures, on the contrary, soft polymer matrices alter the deformation, accommodate the mechanical strain, and dissipate local stress; whereas strain-adaptive Ag NWs percolation pathways adapt to such structural change due to significant mechanical mismatch and therefore preserve interconnected conductive networks

(Fig. 1b). Numerical calculations of tunneling resistance[35,36] among Ag NWs together with finite element analysis (FEA) simulations provided a quantification of the electrical variations (Supplementary Note 1). As shown in Fig. 1e, PSPN exhibits a marginal increase in electrical resistance across a broad range of uniaxial strains, whereas conventional nonporous nanocomposite experiences a rapid resistance increase, followed by an abrupt electrical failure owing to the development and propagation of microscopic cracks within Ag NWs networks. This noticeable disparity signifies a considerably improved stretchability in the porous nanocomposites, showcasing exceptional electrical-mechanical decoupling. Furthermore, we apply theoretical calculation based on three-dimensional (3D) percolation theory[37] to correlate the percolation threshold V_c (i.e., minimum number of conductive fillers required to create conductive pathways) with pore size D_p of the polymer matrix (Supplementary Note 2),

$$V_{P,c} = \frac{1.4093\pi d^2}{Vl} f(D_p)$$

where d and l are the diameter and length of the nanowire, V is the volume of the nanocomposite, $f(D_p)$ is the surface area of the porous microstructure as a function of pore size D_p. The presence of microscale porous structure results in a percolation threshold orders of magnitude lower than that observed in nonporous nanocomposites (Fig. 1f). Besides, the electrical conductivity also depends on D_p of the porous composites (Supplementary Note 3). Despite the low volume fractions of conductive fillers, the PSPN obtained with high electrical conductivity and stretchability consistently aligns with the results of these numerical examinations (Fig. 1g).

Strain-resilient property and ultralow percolation threshold

We experimentally demonstrated the self-assembly of Ag NWs at the interface of a continuous “solid-gas” phase as the concentration of Ag NWs increases (Fig. 2a). Such selective distribution substantially reduces the volume fraction of conductive fillers required for continuous electron transport, in contrast to conventional nonporous nanocomposite where filler materials are nearly homogeneously distributed. To understand the impact of porous microstructures, we quantitatively evaluated the electrical conductivity of PSPN and nonporous nanocomposite as a function of Ag NWs volume fractions. The data in Fig. 2b were fitted using 3D percolation theory (Supplementary Note 4)[38]. We observed a notable reduction in percolation threshold (V_c) from 0.02971 to 0.00131 (a factor of ~22) with the existence of porous microstructures (mean pore size, ~6.4 μm). Based on our theoretical analysis presented in Fig. 1f, we empirically validated that the percolation threshold is influenced by pore size. We note that the addition of 1-butanol as co-nonsolvent allows broader control over pore sizes compared with the porous nanocomposite made with ethanol, when varying the volumetric ratios between PU solution and Ag NWs solution (Supplementary Figs. 2 and 4). Furthermore, there was a 48-fold decrease in the threshold (V_c=0.00062) with an increase in pore size to ~16.8 μm (Supplementary Fig. 5) compared to nonporous nanocomposites. To the best of our knowledge, this is the lowest value ever reported (Supplementary Tables 1 and 2). The electrical conductivity differs depending on

Ag NWs volume fractions, reaching an optimum value of ~642,000 S m^{-1} ($V_{Ag\ NWs}$= ~0.007) after cold welding with saturated sodium chloride or sodium borohydride solution.

The PSPN comprises randomly distributed Ag NWs confined within the porous polymer matrices. The Ag NWs establish conductive percolation networks, effectively bridging interconnected pores across multiple scales (Fig. 2c, left). The significant mechanical mismatch in Young's modulus between soft PU elastomer (~16 MPa) and rigid Ag NWs (~83 GPa) generates anisotropic regions with different elasticity. Upon stretching, local stress dissipation is achieved through autonomous structural alternation of the soft PU elastomer, while the strain-adaptive Ag NWs retain the original percolation networks with minimally altered orientation (Fig. 2c, middle and right). As a result, this enables delayed electrical failure (>600%), and notably stabilized electrical resistance under large uniaxial (R/R_0=1.5 at 100% and 20.2 at 500%; Fig. 2d, and Supplementary Fig. 6), biaxial strains, and bending (Supplementary Fig. 7). In contrast, electrical failure in nonporous nanocomposites occurs at an early stage (~100%), primarily because they lack energy-dissipative porous microstructures, resulting in the rupture of percolation pathways (Supplementary Fig. 8). Our strategy's superiority is further demonstrated by recording electrocardiogram signals using electrical wiring made from our PSPN and conventional Ag NWs (Supplementary Fig. 9 and Video 1).

In Fig. 2e and Supplementary Fig. 10, we compared the evolution of electrical resistance of PSPN with other representative materials. Remarkably, our porous conductor exhibits substantially smaller variations in resistance compared to a variety of porous and nonporous composites. Furthermore, our porous conductor exhibits outstanding durability and reliability, as evidenced by a slight resistance change (R/R_0 =5.4) after cyclic stretching of 50% for 10,000 cycles, in evident contrast to that of the nonporous control (R/R_0 =262, Fig. 2f). The susceptibility to fatigue-induced electrical performance degradation in the nonporous nanocomposite aligns with previous findings on Ag flakes/nanoparticles, which deteriorates abruptly with increased stretching cycles[4]. Such exceptionally durable performance of the porous nanocomposite can also be extended to larger strains (Supplementary Fig. 11). Moreover, we found that alcohol (e.g., ethanol) treatment can facilitate the recovery of electrical resistance following stretching in our porous nanocomposite, whereas negligible effect was observed in the nonporous counterpart (Supplementary Fig. 12). This phenomenon arises from capillary forces generated during ethanol evaporation, which facilitates cold sintering of the inter-nanowire junctions of the Ag NWs[39]. We also demonstrate its resilience to multiple washing cycles (Supplementary Fig. 13) and various damage scenarios, including puncturing with a scalpel knife, impact loading from a hammer strike, twisting and bending (Fig. 2g and Supplementary Video 2). This outstanding performance can be attributed to the energy-dissipating porous PU microstructures, which dampen external mechanical impacts, and the robust interface formed by hydrogen bonding between Ag NWs and PU (Supplementary Fig. 14)[9]. Here, we utilized PSPN with the thickness of ~200 μm to fabricate wireless stretchable bioelectronics. Varying the thickness of PSPN by adjusting the casting solution per unit surface area shows a trivial impact on its electromechanical performance (Supplementary Fig. 15). Notably, our porous conductive nanocomposite also remains electrically stable over 60 days under ambient conditions, 3 hours under ultraviolet/ozone (UV/O_3) treatment, and 30 mins of

wearing with heavy skin perspiration (Supplementary Fig. 16). Besides, we note that the electrical conductivity, modulus, and electromechanical properties of the resulting porous nanocomposites are tunable by varying the volumetric ratios between PU and Ag NWs solutions (Supplementary Fig. 17) and post-annealing temperatures (Supplementary Fig. 18).

Besides, the multiscale interconnected cellular structure enables enhanced porosity and breathability to facilitate skin perspiration and improve long-term biocompatibility. We note a substantial increase in water vapor transmission rate (WVTR) from ~615 to ~4,424 g m^{-2} day^{-1} and reduction in Young's modulus from ~9.1 to ~1.6 MPa in presence of the porous structure (Fig. 2h). Given that the material's elastic modulus E scales with its density ρ, $E/E_s \propto (\rho/\rho_s)^n$ [40], where the power (n) is associated with the porous material's nano/microstructures, we attribute the increased softness to the multiscale nano- and microstructures. This feature promotes a compliant interface with biological tissues[41]. Finally, we provide a comprehensive comparison of our PSPN with other state-of-the-art soft porous and nonporous conductors in terms of percolation threshold, strain-insensitivity, stretchability, electrical conductivity, and breathability. The detailed comparisons are provided in Fig. 2i[2,31,42–45], Supplementary Fig. 10, and Supplementary Tables 1 and 2. It is worth noting that high electrical stability under large strain is achieved by coating liquid metals on fiber mat surfaces[46]. However, this composite faces challenges such as performance degradation during skin rubbing and other limitations inherent in liquid-metal-based composites.

Strain-insensitive wireless powering system

Wireless power delivery is emerging in the realm of wearable and soft electronics, as it eliminates the use of batteries[47–49]. Here we fabricate stretchable spiral coils using our PSPN and implement in a radiofrequency (RF) wireless power transfer (WPT) system. Fig. 3a shows the two-port network model of the WPT system, and the magnetic field distribution of the transmitter and receiver coils under RF excitation. To evaluate the performance of the PSPN in wireless communication technology, we first theoretically examined the magnetic field distribution using Ansys Maxwell simulation (Fig. 3b). Despite comparable performances in unstretched state, the porous coil remains largely unchanged, while the nonporous one experiences a significant reduction in magnetic field at 50% strain. This is ascribed to the stable electrical resistance and inductance of PSPN coils under strain (Fig. 3c and Supplementary Fig. 19) and bending (Supplementary Fig. 20).

Accordingly, we experimentally measured the variations of scattering parameters S_{11}, S_{21}, and the transfer efficiency η of the WPT system across uniaxial strains (Figs. 3d–f). We note slight change in these parameters for up to 100% strain. Also, Advanced Design System (ADS) simulation indicates the strain-insensitive feature of the induced voltage on the stretchable PSPN coil (Fig. 3f inset). The extracted transfer efficiency of the stretchable WPT system at 50 MHz reduces slightly from 76.0% to 74.8% at 50% strain and further to 66.6% at 100% strain (Fig. 3g). This arises primarily from the altered coupling strength caused by geometry changes between the two coils. Notably, our device outperformed Ag NWs nanofiber-based antenna[50]. Conversely, the coils' efficiency for nonporous composite

dropped sharply to 23.1% at 25% strain, with a total loss of power transfer capability by 50% strain (Fig. 3g and Supplementary Fig. 21). As anticipated, a shorter distance between the coils notably boosts transfer efficiency (Fig. 3h).

NFC-based wireless powering and data transmission systems enable a myriad of new applications for wearable and implantable bioelectronic devices[48,51,52]. These devices, however, rely on intrinsically rigid materials with limited stretchability (<30%), which falls short of meeting the strain tolerance requirement for certain skin-interfaced devices (>80%)[53]. We fabricated wearable wireless power transmitters and implantable receivers based on PSPN. We first theoretically evaluated the transmitter coil's performance to power a device implanted in a body phantom, constructed from a glass cylinder filled with 1% agarose gel (Fig. 4a and Supplementary Fig. 22). Electromagnetic (EM) simulations reveal that the inherently soft nanocomposite coil seamlessly adapts to curved body contours. This adaptability facilitates deeper penetration of EM power into the body, resulting in superior power delivery compared to its rigid counterparts (Fig. 4b and Supplementary Fig. 23). Experiments reveal that the coupling coefficient κ diminishes with increasing lateral and vertical separation between the coils (Fig. 4c). Moreover, the soft conformal coil exhibits higher coupling coefficients than conventional rigid coil at all radii (Fig. 4d). Additionally, we note that the transfer efficiency (radius, 5.5 cm; implantation depth, 1 cm) remains stable (>33%) at 50 MHz within 100% tensile strain (Fig. 4e). To evaluate the wireless powering further, we used the PSPN transmitter coil to power an implanted red light-emitting diode (LED) in fish (Fig. 4f). Quantitative analysis of the LED brightness suggests reliable and stable operation of the PSPN coil at 50% strain. In contrast, the conventional Ag NWs coil degrades rapidly upon stretching, failing electrically at just 20% strain (Fig. 4g).

To further explore PSPN's potential as an implantable receiver coil, we developed a wireless optoelectronic system comprising an implantable energy harvesting device that captures RF signal from an external transmitter, processes the signal through voltage multiplier, and subsequently routes the generated direct current (DC) voltage to illuminate a red LED (Supplementary Fig. 24). We encapsulated the device with silicone elastomer (Smooth-on, Inc.) and deployed between the skin and muscle (subcutaneously) on the ventral side of a mouse while under isoflurane anesthesia (Fig. 4h). There were negligible degradations when stored in phosphate-buffered saline (PBS, pH 7.4) and artificial perspiration (pH 4.3, Pickering Laboratories) for nine days at room temperature (Supplementary Fig. 25). The wireless powering system thus enables real-time, precise control of illumination for freely moving mice (Fig. 4i and Supplementary Videos 3,4).

Wireless and multiplexed biochemical sensing

Furthermore, we fabricated a fully stretchable wireless bioelectronic system for multiplexed biochemical sensing. Our battery-free bioelectronic platform comprises a stretchable biochemical sensing interface and a spiral coil as the coupling unit for wireless data transmission (Fig. 5a). The design principle relies on a modularized inductor-capacitor (LC) resonance circuit model where varactors convert electrical potential variations into capacitance modulations (Fig. 5b). These modulations directly correspond with the resonance frequency f_s of the LC circuit, as described by:

$$f_s = \frac{1}{2\pi\sqrt{LC}}$$

where L and C are the equivalent inductance and capacitance of the resonance circuit, respectively. When targeted analytes are present, the potential difference between the working and reference electrodes of the biochemical sensors corresponds to a frequency shift. Since f_s is an intrinsic property of the resonance circuit, it allows for robust and reliable wireless data transmission. This was exemplified by high-fidelity measurement of a wealth of ions, including Na^+, K^+, NH_4^+, and H^+ (Fig. 5c, d and Supplementary Fig. 26). The obtained readouts exhibit linear relationship with high sensitivities of 0.66, 0.61, 0.67, and 1.04 MHz/decade, respectively. To achieve multiplexed sensing of biomarkers to capture biometric signature profiles with a minimum level of crosstalk, we carefully chose capacitors in the resonance circuit, producing distinct resonance dips at approximately 38, 55, and 80 MHz. Varying a single analyte in the solution primarily affects its corresponding f_s, with minimal shifts in other sensors, highlighting remarkable selectivity against interfering ions (Supplementary Fig. 27).

When the PSPN sensing device was subjected to uniaxial tensile stretch, a strain insensitivity of less than 10% performance variation is observed when stretched up to 50% strain, i.e., from 0.68 to 0.62 MHz/decade (Fig. 5e, f). Such changes largely stem from alterations in device geometry, which weaken the coupling strength. Conversely, the device made of conventional nonporous Ag NWs exhibited stark instability under strain, causing a sensitivity reduction from 0.64 to 0.45 MHz/decade at 15% and becoming non-operational at 20% (Fig. 5f and Supplementary Fig. 28). Furthermore, the devices maintained their initial performance across repetitive strain cycles, with only ~3% and ~5% sensitivity changes after 1,000 cycles at 25% and 50% strains, respectively (Fig. 5g).

We constructed a multiplexed wireless sensing system integrating glucose and alcohol sensors with high sensitivities of 1.79 and 0.014 MHz/mM respectively (Fig. 5h–j). These developed sensors showcased minimal signal fluctuations even when introduced to a range of interfering biomarkers (Fig. 5k and Supplementary Fig. 29). Notably, our wireless sensing system remains stable in physiologically relevant temperature range (Supplementary Fig. 30). Our wireless sensor prototype forms intimate interface with human skin due to the absence of on-chip integrated circuits (Fig. 5l). This battery-free device facilitates continuous, real-time perspiration monitoring during everyday activities (Fig. 5m). For example, we monitored the evolutions of glucose and ethanol concentrations in perspiration over a course of eight hours. We observed a notable rise and subsequent rapid decline in glucose levels—with alcohol levels remaining largely unchanged—post the first meal between 0–3 h (Fig. 5n and o). Furthermore, the two biomarkers exhibited nearly synchronized variations following a combined intake of a meal and a drink (1.2 g of white wine (50% alcohol by volume) per 1 kg of the volunteer’s body weight).

Conclusions

We also note that the phase separation technique can be potentially extended to other conductive nanofillers, such as carbon nanotubes (Supplementary Fig. 31). These findings suggest that the phase separation approach could open up new avenues for constituent materials across diverse domains. Future research should focus on exploring new manufacturing technologies (e.g., additive manufacturing) that are compatible with this technique to enable scalable production. Additionally, the development of strain-insensitive, NFC-based wireless bioelectronics with customized biosensing and therapeutic modules holds promise for a variety of healthcare applications.

Methods

Our research complies with all relevant ethical regulations. Specifically, all animal procedures were performed in accordance with the National Institutes of Health Guide for the Care and Use of Laboratory Animals and approved by the University of Missouri Animal Care and Use Committee. The on-body evaluations of skin-interfaced devices on human participants were conducted under approval from Institutional Review Board at the University of Missouri-Columbia (number 2010272). All human subjects gave written and informed consent before participation in the studies. The healthy participant (age 28; male) were recruited from MU campus through word of mouth.

Materials.

Bis(2-ethylehexyl) sebacate (DOS), 1-butanol, sodium tetrakis[3,5-bis(trifluoromethyl)phenyl] borate (Na-TFPB), polyvinyl chloride (PVC), sodium tetraphenylborate (NaTPB), cyclohexanone, polyvinyl butyral (BUTVAR B-98, PVB), NH_4^+ ionophore (nonactin), alcohol oxidase, bovine serum albumin, NaCl, KCl, NH_4Cl were purchased from Sigma Aldrich. Polyaniline base, acetic acid, dimethyl sulfoxide (DMSO), THF, cyclohexanone, PBS solution, and dextrose (D-glucose) were obtained from Fisher Scientific. Glucose Oxidase was acquired from Toyobo Corp. Ag/AgCl ink was purchased from CH Instruments, Inc.

Synthesis of PSPN and device fabrications.

The phase-separated porous Ag NWs nanocomposites were prepared by mixing PU (Texin®RxT85A, Covestro) solution (in THF) with Ag NWs solution (20 mg/ml in ethanol; Ag NW-40, ACS Material) at various concentrations and volume ratios. Drop-casting the nanocomposite precursor solution on aluminum foils and drying under ambient conditions (~3 hours) completed the fabrication of highly conductive PSPN film. Note that the electrical conductivity, stretchability, and electrical-mechanical decoupling are tunable based on the concentrations and volume ratios of constituent materials. PSPN denotes PSPN made from ethanol-based Ag NWs solution, whereas PSPN with 1-butanol represents that made with the co-addition of 1-butanol to control pore sizes (Supplementary Fig. 4). The optimum porous nanocomposite was prepared by mixing 5 g of PU solution (90 mg/ml) with 4.5 ml of Ag NWs solution (20 mg/ml) and was used throughout the study unless otherwise stated. Similarly, porous PU substrates were also fabricated by mixing 50 ml of PU solution (70

mg/ml in THF) with 40 ml of 1-butanol and dried under ambient conditions. The nonporous Ag NWs nanocomposite was fabricated by mixing PU (HydroMed D3, AdvanSource Biomaterial) solution (ethanol:water=9:1) with Ag NWs solution (20 mg/ml in ethanol). Conventional Ag NWs was fabricated by spray-coating Ag NWs onto oxygen plasma-treated elastomeric PU substrate. Laser cutting using a VLS2.30 universal laser system defines desired patterns. Stretchable wireless NFC antenna was obtained by transferring pre-designed spiral PSPN coils, assisted by Aquasol water-soluble tape, to the porous PU substrates. Waterborne PU adhesive (HydroMed D3, AdvanSource Biomaterial) allows for strong and robust interface under strain between PSPN and the substrate.

Fabrication of biochemical sensors

We first fabricated soft and stretchable sensors (3 mm diameter) by transfer-printing of laser-induced graphene (LIG) electrodes onto PU elastomer substrates. Specifically, the LIG electrodes were engraved on a polyimide (PI) film using a 30 W CO_2 laser cutter (power, 12%; speed, 15%; VLS2.30 universal laser systems). Next, PU solution (Texin®RxT85A, 40 mg/ml in THF) was applied and dried at room temperature. Careful transfer-printing from PI film to PU elastomer completed the process. Sodium ion sensor was prepared by drop-casting 10 μl of Na^+ selective membrane solution (1 mg of Na ionophore, 0.55 mg of Na-TFPB, 33 mg of PVC, and 65.45 mg of DOS in 660 μl of THF) on the graphene electrode. Potassium sensor was prepared by drop-casting 6 μl of K^+ selective membrane solution (2 mg of valinomycin, 0.5 mg of NATPB, 32.7 mg of PVC, and 64.7 mg of DOS in 350 μl of cyclohexanone) on each LIG electrode. The NH_4^+ sensor was fabricated by drop-casting 6 μl of NH_4^+ selective membrane solution [1 mg of NH_4^+ ionophore (nonactin), 33 mg of PVC and 66 mg of DOS in THF] on the LIG electrode. Next, pH sensor was prepared by drop-casting 10 μl of the polyaniline base solution (20 mg/ml in DMSO) on the LIG electrode and dried at 80 °C, followed by 15 min of incubation in 1.0 M HCl. To prepare enzyme-based sensors, gold nanoparticles (25 nm) was first sputter-coated on the LIG electrodes, 5 μl of cocktail (10 mg of Prussian blue and 5 mg of chitosan dissolved in 1 ml of 0.1 M acetic acid) was then drop-casted. Next, 5 μl of enzyme solution was added and dried at 4 °C overnight, followed by addition of 3 μl of 0.5% Nafion solution. Here, the glucose oxidase solution was prepared by mixing glucose oxidase (10 mg/ml in PBS) with chitosan/CNT solution (1% chitosan and 5 mg/ml of MWCNT in 0.1 M acetic acid) at a volume ratio of 1:1. The alcohol oxidase solution was composed of alcohol oxidase, bovine serum albumin (10 mg/ml in PBS) and chitosan (1% in 0.1 M acetic acid) with a volume ratio of 8:1:1. Reference electrode was prepared by first applying a layer of Ag/AgCl paste onto the LIG electrode, followed by the addition of 3 μl of PVB solution (79.1 mg of PVB and 50 mg of NaCl in 1 ml of methanol).

Characterizations and measurements.

SEM images were taken with a FEI Quanta 600 FEG Environmental SEM. Water vapor transmission rates were determined based on ASTM96 at 35 °C. Mechanical properties were characterized using a Mark-10 ESM303 tensile tester. Electrical conductance was measured by a digital source meter (2604B, Keithley Instruments). Fourier transform infrared spectra were obtained using a spectrometer (Nicolet 6700; Thermo Electron Corporation).

Electrocardiogram signals were recorded with PowerLab T26 (AD Instruments). Statistical analyses were carried out using Origin 2016 software.

Coil design and numerical simulations.

The spiral coils for wearable WPT applications (Fig. 3, Figs. 4b–g, and Supplementary Figs. 19–23) were custom-designed with 8-mm inner radius, 2 turns, 5-mm trace, and 1-mm spacing. The implantable receiver coils (Fig. 4h, i and Supplementary Fig. 24) feature 5.5-mm inner radius, 5 turns, 1.5-mm trace, and 0.3-mm spacing. The sensing coils for monitoring ions and metabolites (Fig. 5) are characterized by a 4-mm inner radius, 4 turns, a 1.5-mm trace width, and a 0.3-mm spacing. The magnetic field distributions for the WPT system (Fig. 3a), the coil under strain (Fig. 3b), and the coil placed on human body (Fig. 4b and Supplementary Fig. 23) were simulated by using Ansys Maxwell. Particularly, for Fig. 4b and Supplementary Fig. 23, the human body was modeled by a stratified composition of a 1-mm skin layer with relative permittivity of 43 and relative permeability of 1, a 2-mm adipose layer with relative permittivity of 5.28 and relative permeability of 1, and a 7-mm bone layer with relative permittivity of 11.4 and relative permeability of 1. Notably, due to the unit permeability of those materials, the presence of human tissue barely affects the performance of the WPT system. The RF system simulations (inset of Fig. 3f) were performed by Advanced Design System (ADS).

RF properties characterization and measurements.

The equivalent inductance (L), resistance (R), and Q-factor of the coil were obtained by directly connecting the coil to a vector network analyzer (VNA; N5242B PNA-X Network Analyzer, Keysight) and measuring the input impedance Z_{in}. The L, R, and Q values could be extracted from Z_{in} according to the following equation:

$$L = \frac{Im(Z_{in})}{2\pi f}$$

$$R = Re(Z_{in})$$

$$Q = \frac{Im(Z_{in})}{Re(Z_{in})} = \frac{2\pi f L}{R}$$

where $Im(Z_{in})$ and $Re(Z_{in})$ are the imaginary and real parts of the input impedance Z_{in}, respectively, and f is the frequency. For WPT applications, the scattering parameters (S_{11} and S_{21}) and impedance parameters (Z_{11}, Z_{12}, and Z_{22}) of the two-port network were also measured by the Keysight PNA-X VNA. The power transfer efficiency η could be derived from the scattering parameters and the coupling coefficient κ could be obtained from the impedance parameters. The brightness of LED for demonstrating power transfer efficiency was measured by a light meter (ET130, Klein Tools). A portable VNA (LibreVNA) was used for continuous, real-time perspiration monitoring. Common-cathode varactors MAVR-000409-0287FT, MAVR-000405-0287FT, and MAVR-045441-0287AT from Macom

were used for achieving resonances at around 38, 55, and 80 MHz, respectively. The power transfer efficiency η is given by:

$$\eta = \frac{|S_{21}|^2}{1 - |S_{11}|^2}$$

where S_{21} and S_{11} are the transmission and reflection coefficients of the two-port network. The coupling coefficient, κ, representing the fraction of magnetic flux between the transmitter and receiver coils, is given by

$$\kappa = \frac{M}{\sqrt{L_1 L_2}} = \frac{Im(Z_{12})}{\sqrt{Im(Z_{11})Im(Z_{22})}},$$

where M is the mutual inductance between the two coils, $Im(Z_{11})$, $Im(Z_{12})$, and $Im(Z_{22})$ are the imaginary components of the two-port network's impedance parameters.

Implantation of stretchable wireless optoelectronic device.

Adult female Swiss Webster mice (10-14 weeks old, Charles River) were used for surgical implantation of the device. Mice were group housed in cages (20-26 °C, 30-70% humidity) on a 12:12-h light-dark cycle and fed a standard chow diet ad libitum. The whole device was first sterilized using ethanol, then the device was implanted between the skin and muscle (subcutaneously) on the ventral side of the animal while under isoflurane anesthesia. Prior to implantation, a small incision was made on the lateral side of the animal and the skin was separated from the abdominal muscle with blunt forceps. After implantation, skin was closed with sutures and the animal was allowed to recover from anesthesia.

Data Availability

The main data supporting the results in this study are available within the paper and its Supplementary Information. Source data for Figs. 1–5 is provided with this paper.

Supplementary Material

Refer to Web version on PubMed Central for supplementary material.

Acknowledgments

Z.Y. acknowledges the financial support from the start-up fund of the University of Missouri-Columbia. Z.Y., P.C., and J.X. acknowledge National Institute of Biomedical Imaging and Bioengineering (award number: R01EB033371). The human study was supported by Z.Y.'s start-up fund. W.G. acknowledges support from National Institutes of Health grants (R01HL155815 and R21DK13266). P.C. acknowledges the financial support from NSF ECCS CAEER 1914420. I.O. also acknowledges the financial support from the start-up fund of the University of Missouri-Columbia.

Reference

1. Jung D et al. Highly conductive and elastic nanomembrane for skin electronics. Science 373, 1022–1026 (2021). [PubMed: 34446604]

2. Choi S et al. Highly conductive, stretchable and biocompatible Ag-Au core-sheath nanowire composite for wearable and implantable bioelectronics. Nat. Nanotechnol 13, 1048–1056 (2018). [PubMed: 30104619]

3. Lee W et al. Universal assembly of liquid metal particles in polymers enables elastic printed circuit board. Science 378, 637–641 (2022). [PubMed: 36356149]

4. Matsuhisa N et al. Printable elastic conductors by in situ formation of silver nanoparticles from silver flakes. Nat. Mater 16, 834–840 (2017). [PubMed: 28504674]

5. Veerapandian S et al. Hydrogen-doped viscoplastic liquid metal microparticles for stretchable printed metal lines. Nat. Mater 20, 533–540 (2021). [PubMed: 33398123]

6. Hui Y et al. Three-dimensional printing of soft hydrogel electronics. Nat. Electron 5, 893–903 (2022).

7. Jiang Z et al. A 1.3-micrometre-thick elastic conductor for seamless on-skin and implantable sensors. Nat. Electron 5, 784–793 (2022).

8. Zhao Y et al. A self-healing electrically conductive organogel composite. Nat. Electron 6, 206–215 (2023).

9. Jiang Z et al. Highly stretchable metallic nanowire networks reinforced by the underlying randomly distributed elastic polymer nanofibers via interfacial adhesion improvement. Adv. Mater 31, 1903446 (2019).

10. Luo Y et al. Technology roadmap for flexible sensors. ACS Nano 17, 5211–5295 (2023). [PubMed: 36892156]

11. Wang C, He T, Zhou H, Zhang Z & Lee C Artificial intelligence enhanced sensors-enabling technologies to next-generation healthcare and biomedical platform. Bioelectron. Med 9, 17 (2023). [PubMed: 37528436]

12. Choi S, Han SI, Kim D, Hyeon T & Kim D-H High-performance stretchable conductive nanocomposites: materials, processes, and device applications. Chem. Soc. Rev 48, 1566–1595 (2019). [PubMed: 30519703]

13. Sim K, Rao Z, Ershad F & Yu C Rubbery electronics fully made of stretchable elastomeric electronic materials. Adv. Mater 32, 1902417 (2020).

14. Gao W et al. Fully integrated wearable sensor arrays for multiplexed in situ perspiration analysis. Nature 529, 509–514 (2016). [PubMed: 26819044]

15. Yang Y & Gao W Wearable and flexible electronics for continuous molecular monitoring. Chem. Soc. Rev 48, 1465–1491 (2019). [PubMed: 29611861]

16. Kim JJ et al. Skin electronics: next-generation device platform for virtual and augmented reality. Adv. Funct. Mater 31, 2009602 (2021).

17. Yamagishi K, Zhou W, Ching T, Huang SY & Hashimoto M Ultra-deformable and tissue-adhesive liquid metal antennas with high wireless powering efficiency. Adv. Mater 33, 2008062 (2021).

18. Zhuang Q et al. Wafer-patterned, permeable, and stretchable liquid metal microelectrodes for implantable bioelectronics with chronic biocompatibility. Sci. Adv 9, eadg8602 (2023). [PubMed: 37256954]

19. Jung D et al. Adaptive self-organization of nanomaterials enables strain-insensitive resistance of stretchable metallic nanocomposites. Adv. Mater 34, 2200980 (2022).

20. Wang T, Liu Q, Liu H, Xu B & Xu H Printable and highly stretchable viscoelastic conductors with kinematically reconstructed conductive pathways. Adv. Mater 34, 2202418 (2022).

21. Kim SH et al. An ultrastretchable and self-healable nanocomposite conductor enabled by autonomously percolative electrical pathways. ACS Nano 13, 6531–6539 (2019). [PubMed: 31072094]

22. Sun B et al. Gas-permeable, multifunctional on-skin electronics based on laser-induced porous graphene and sugar-templated elastomer sponges. Adv. Mater 30, 1804327 (2018).

23. Yi H et al. Constructing high-performance 3D porous self-standing electrodes with various morphologies and shapes by a flexible phase separation-derived method. J. Mater. Chem. A 7, 22550–22558 (2019).

24. Wang Y, Yokota T & Someya T Electrospun nanofiber-based soft electronics. NPG Asia Mater. 13, 22 (2021).

25. Zhu D, Handschuh-Wang S & Zhou X Recent progress in fabrication and application of polydimethylsiloxane sponges. J. Mater. Chem. A 5, 16467–16497 (2017).
26. Yao S et al. Ultrasoft porous 3D conductive dry electrodes for electrophysiological sensing and myoelectric control. Adv. Mater. Technol 7, 2101637 (2022). [PubMed: 36276406]
27. Zhou W et al. Gas-permeable, ultrathin, stretchable epidermal electronics with porous electrodes. ACS Nano 14, 5798–5805 (2020). [PubMed: 32347707]
28. Wang F et al. Progress report on phase separation in polymer solutions. Adv. Mater 31, 1806733 (2019).
29. Hołda AK & Vankelecom IF Understanding and guiding the phase inversion process for synthesis of solvent resistant nanofiltration membranes. J. Appl. Polym. Sci 132, 42130 (2015).
30. Mandal J et al. Hierarchically porous polymer coatings for highly efficient passive daytime radiative cooling. Science 362, 315–319 (2018). [PubMed: 30262632]
31. Zhu H-W et al. Printable elastic silver nanowire-based conductor for washable electronic textiles. Nano Res. 13, 2879–2884 (2020).
32. Lee HJ, Jung B, Kang YS & Lee H Phase separation of polymer casting solution by nonsolvent vapor. J. Membr. Sci 245, 103–112 (2004).
33. Sun X, Sun G & Wang X Morphology modeling for polymer monolith obtained by non-solvent-induced phase separation. Polymer 108, 432–441 (2017).
34. Binks B & Lumsdon S Pickering emulsions stabilized by monodisperse latex particles: effects of particle size. Langmuir 17, 4540–4547 (2001).
35. Hu N, Karube Y, Yan C, Masuda Z & Fukunaga H Tunneling effect in a polymer/carbon nanotube nanocomposite strain sensor. Acta Mater. 56, 2929–2936 (2008).
36. Amjadi M, Pichitpajongkit A, Lee S, Ryu S & Park I Highly stretchable and sensitive strain sensor based on silver nanowire–elastomer nanocomposite. ACS Nano 8, 5154–5163 (2014). [PubMed: 24749972]
37. Li J et al. Correlations between percolation threshold, dispersion state, and aspect ratio of carbon nanotubes. Adv. Funct. Mater 17, 3207–3215 (2007).
38. Taherian R Development of an equation to model electrical conductivity of polymer-based carbon nanocomposites. ECS J. Solid State Sci. Technol 3, M26 (2014).
39. Liu Y et al. Capillary-force-induced cold welding in silver-nanowire-based flexible transparent electrodes. Nano Lett. 17, 1090–1096 (2017). [PubMed: 28094950]
40. Zheng X et al. Ultralight, ultrastiff mechanical metamaterials. Science 344, 1373–1377 (2014). [PubMed: 24948733]
41. Liu S, Rao Y, Jang H, Tan P & Lu N Strategies for body-conformable electronics. Matter 5, 1104–1136 (2022).
42. Kim Y et al. Stretchable nanoparticle conductors with self-organized conductive pathways. Nature 500, 59–63 (2013). [PubMed: 23863931]
43. Boland CS et al. Sensitive electromechanical sensors using viscoelastic graphene-polymer nanocomposites. Science 354, 1257–1260 (2016). [PubMed: 27940866]
44. Sun H, Han Z & Willenbacher N Ultrastretchable conductive elastomers with a low percolation threshold for printed soft electronics. ACS Appl. Mater. Interfaces 11, 38092–38102 (2019). [PubMed: 31566949]
45. Liu Y, Ji X & Liang J Rupture stress of liquid metal nanoparticles and their applications in stretchable conductors and dielectrics. npj Flex. Electron 5, 11 (2021).
46. Ma Z et al. Permeable superelastic liquid-metal fibre mat enables biocompatible and monolithic stretchable electronics. Nat. Mater 20, 859–868 (2021). [PubMed: 33603185]
47. Chung HU et al. Binodal, wireless epidermal electronic systems with in-sensor analytics for neonatal intensive care. Science 363, eaau0780 (2019). [PubMed: 30819934]
48. Ouyang W et al. A wireless and battery-less implant for multimodal closed-loop neuromodulation in small animals. Nat. Biomed. Eng 7, 1252–1269 (2023). [PubMed: 37106153]
49. Jiang Y et al. Wireless, closed-loop, smart bandage with integrated sensors and stimulators for advanced wound care and accelerated healing. Nat. Biotechnol 41, 652–662 (2023). [PubMed: 36424488]

50. Zhang Y et al. High precision epidermal radio frequency antenna via nanofiber network for wireless stretchable multifunction electronics. Nat. Commun 11, 5629 (2020). [PubMed: 33159080]

51. Liu T-L et al. Battery-free, tuning circuit–inspired wireless sensor systems for detection of multiple biomarkers in bodily fluids. Sci. Adv 8, eabo7049 (2022). [PubMed: 35857473]

52. Park SI et al. Soft, stretchable, fully implantable miniaturized optoelectronic systems for wireless optogenetics. Nat. Biotechnol 33, 1280–1286 (2015). [PubMed: 26551059]

53. Someya T, Bao Z & Malliaras GG The rise of plastic bioelectronics. Nature 540, 379–385 (2016). [PubMed: 27974769]

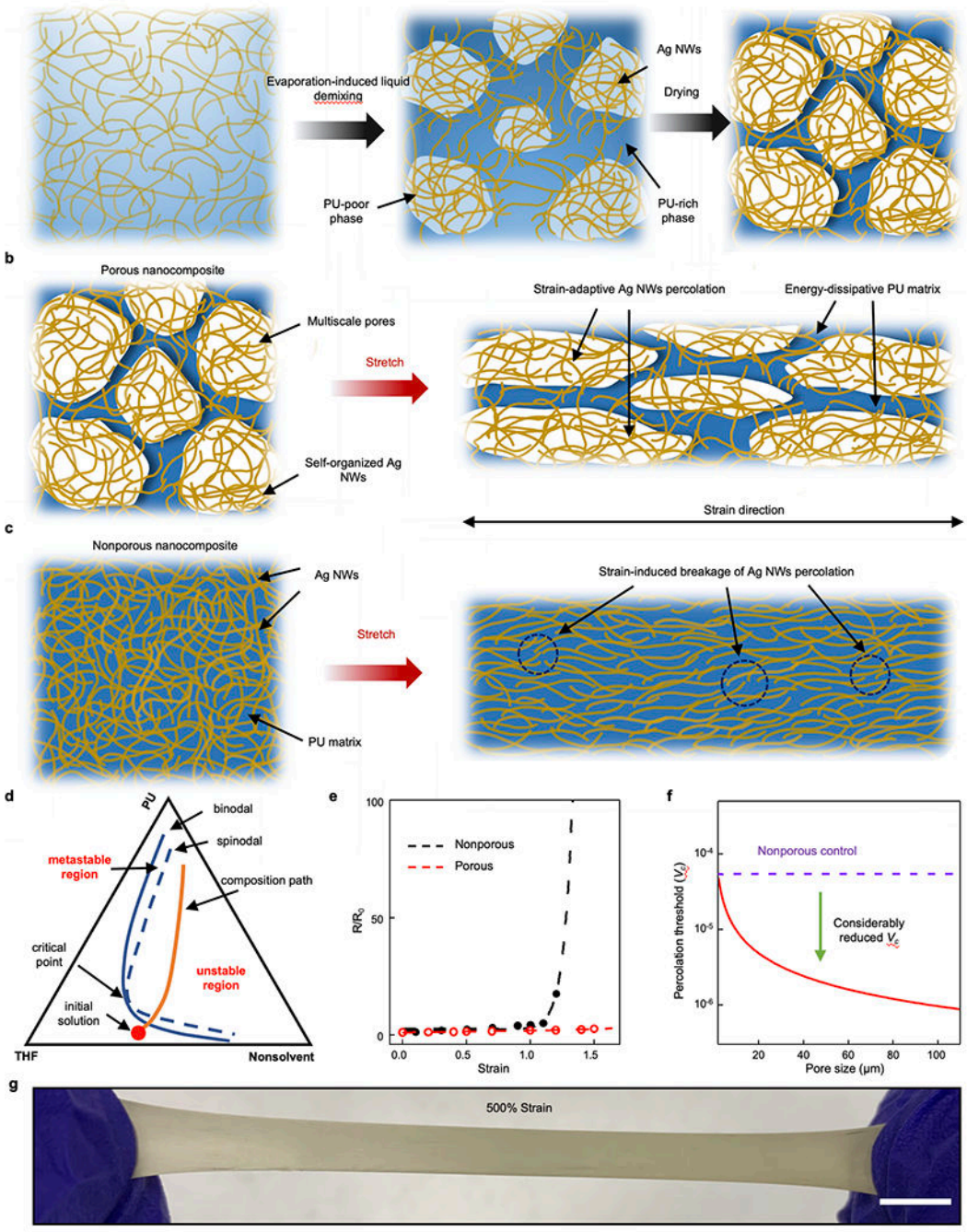

Fig. 1. Schematic and fabrication of strain insensitive PSPN with ultralow percolation thresholds.

a, Schematic illustration of a cross-sectional view of the phase-separation process. **b**, **c**, Schematic of porous (**b**) and nonporous (**c**) Ag NWs nanocomposites at original (left) and stretched (right) states. **d**, Schematic illustration of the isothermal ternary phase diagram of polymer, solvent, and nonsolvent (i.e., PU, THF, and ethanol). The composition path in the phase diagram illustrates the trajectory of the multi-component system as it transitions across various phases due to the evaporation of the solvent and nonsolvent. The initial solution represents the composition of the original casting solution at the outset of this

process. In brief, the initial casting solution, composed of solvent, nonsolvent, and polymer, forms a homogeneous solution. Upon the evaporation of solvent and nonsolvent, the trajectory of the composition path crosses the binodal and spinodal, entering the unstable region where liquid-liquid demixing occurs (two phases). The spinodal decomposition reduces the free energy of the system through diffusion and fluid flow or convection. Such mass transfer leads to the formation of bicontinuous porous structures. **e**, Numerical calculation of evolutions of electrical resistances as a function of applied strain on nonporous (black) and porous (red) nanocomposites. Dashed lines depict the exponentially fitted data. **f**, Theoretical calculation of percolation thresholds for nonporous (purple) and porous (red) Ag NWs nanocomposites, demonstrating its dependency on pore sizes. **g**, Optical photograph of a 500% stretched, free-standing PSPN. Scale bar, 1 cm.

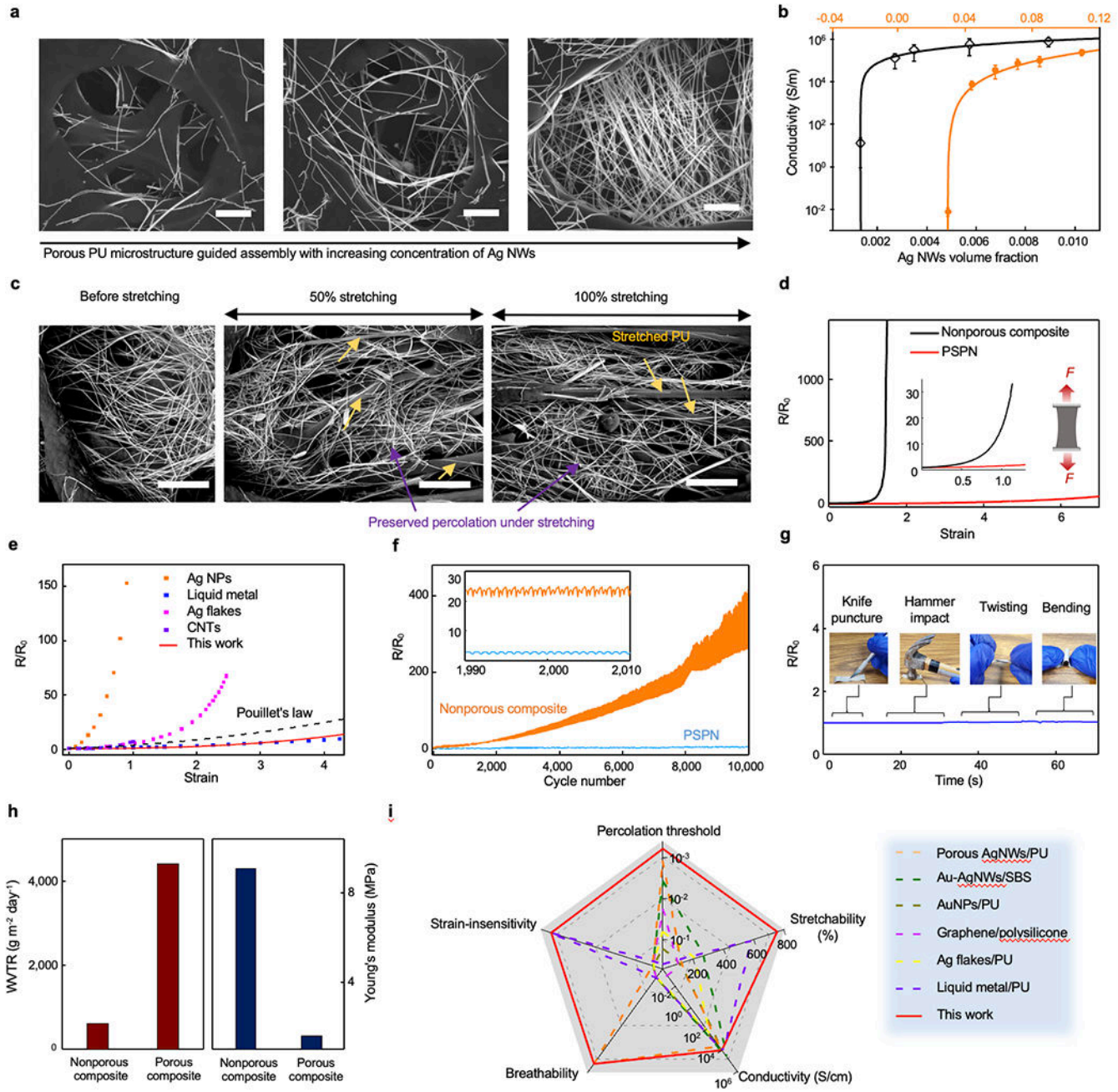

Fig. 2. Phase separation, electrical and mechanical characterizations.

a, Scanning electron microscope (SEM) micrographs of PSPN with increased Ag NWs concentrations. Scale bars, 2 μm. **b**, Electrical conductivities of nonporous composite (orange) and PSPN (black, pore size, ~6.4 μm) as a function of Ag NWs volume fractions. Error bars represent standard deviations of the mean from six samples. Data are fitted using the 3D percolation theory. **c**, SEM images of PSPN before (left) and after stretching (middle, 50%; right, 100%). Scale bars, 5 μm. **d**, Relative resistance change (R/R_0) of nonporous (black) and porous (red) Ag NWs nanocomposites as a function of uniaxial strains. **e**, Comparison of electromechanical characteristics with other reported elastic conductors.

Data were extracted from prior reports as summarized in Supplementary Fig. 10. **f**, Relative resistance changes of nonporous (orange) and porous (blue) nanocomposites subjected to cyclic stretching (50% maximum strain) for 10,000 cycles. Inset shows magnified resistance variations over a 20-cycle period. **g**, Demonstration of PSPN resilience to punctures from a scalpel knife, hammer impact, twisting, and bending. **h**, Water vapor transmission rate (WVTR, left) and Young's modulus (right) of nonporous nanocomposites and PSPN, illustrating substantial increase in breathability and reduction in modulus with the presence of porous microstructures. **i**, Radar chart of the characteristics of this work compared with other soft conductive composites. Note that breathability and strain-insensitivity are qualitative values. Detailed comparison can be found in Supplementary Tables 1 and 2. In short, our PSPN exhibits a distinctive combination of multiple desired features, such as ultralow percolation threshold, outstanding strain-insensitive electrical conductance, high stability, and others, which represents a valuable addition to existing conductive composites for stretchable electronics. The nonporous composites in (**d**) and (**f**) were achieved by collapsing the porous microstructure of PSPN with THF vapor treatment (60 °C, overnight).

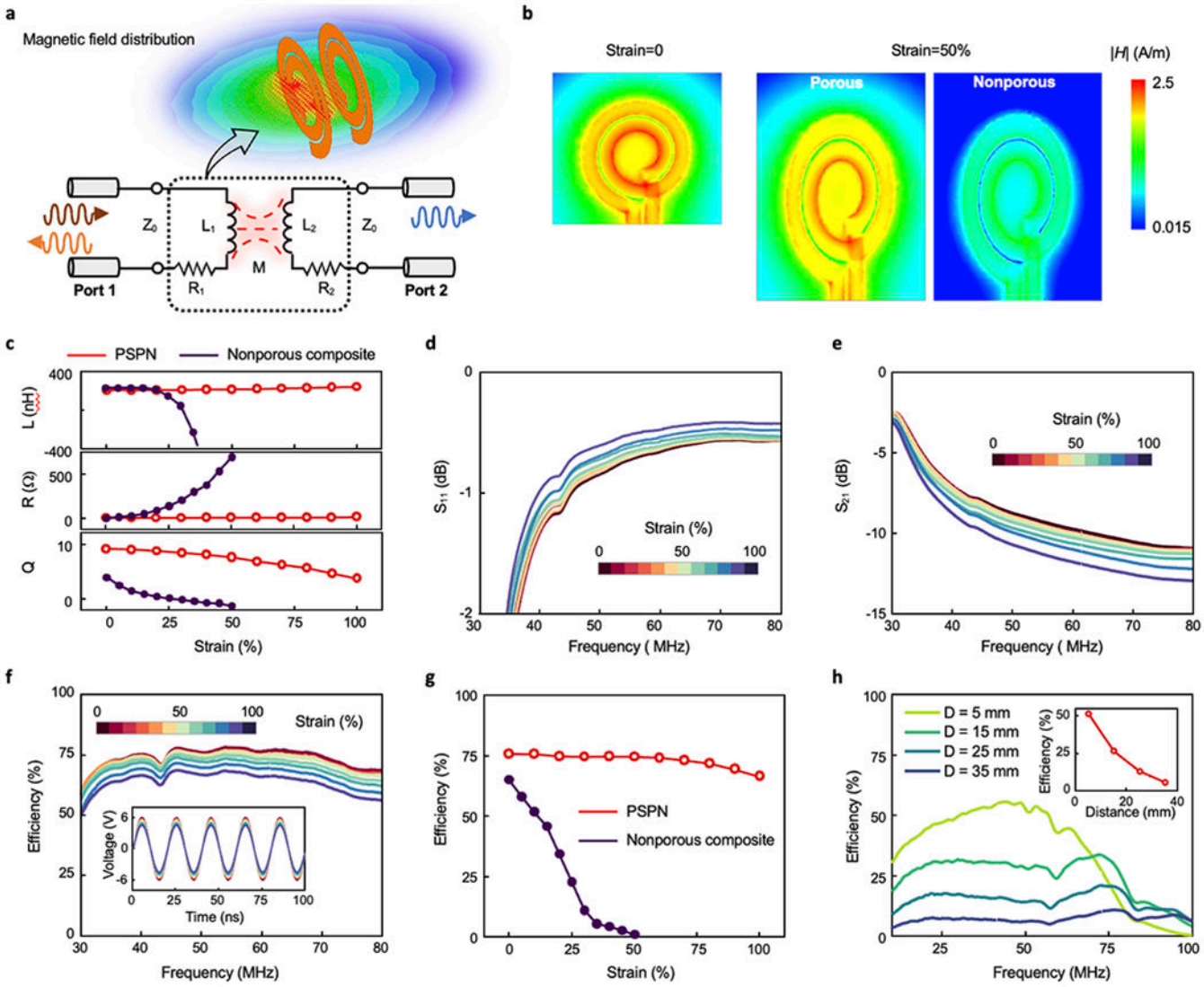

Fig. 3. Radiofrequency properties of the stretchable PSPN coils under tensile strain.

a, Two-port network model of the stretchable wireless power transfer system with the corresponding magnetic field distribution. **b**, Numeric simulations of magnetic field distributions of the porous and nonporous nanocomposites under 50% strain. **c**, Inductance L, resistance R, and quality factor Q of porous (red circle) and nonporous (naval solid) nanocomposites at 50 MHz as functions of uniaxial tensile strains. **d-f**, Scattering parameters S_{11} (**d**), S_{21} (**e**), and power transfer efficiency η (**f**) of the two-port wireless power transfer system comprising a primary transmitter coil and a stretchable receiver coil made from PSPN under strain. Inset in **f**, theoretical calculations of induced voltage on the stretchable receiver coil at 50 MHz under strain. **g,** The evolutions of power transfer efficiency at 50 MHz of the PSPN (red circle) and nonporous nanocomposites (naval solid) as a function of tensile strain. **h**, Power transfer efficiency between the primary transmitter and porous nanocomposite receiver coils at various vertical distances. Extracted data at 50 MHz appears in the inset.

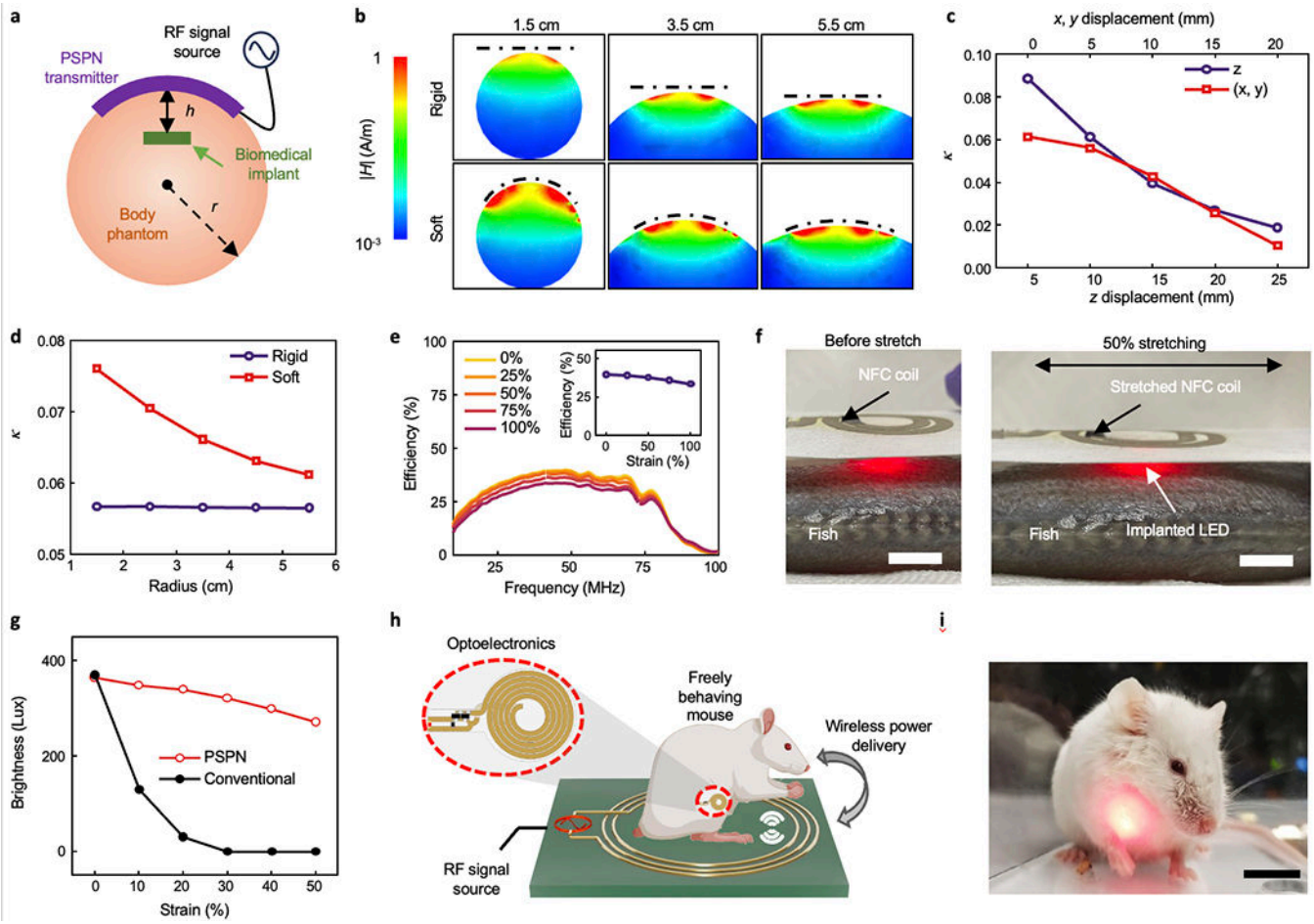

Fig. 4. Stretchable wireless powering system for wearable and implantable bioelectronics.

a, **b**, Schematic of a simplified structure (**a**) and Maxwell simulations (**b**) of magnetic field generated by a rigid (top) and soft transmitter (bottom) placed on various body parts with diameters of 1.5, 3.5 and 5.5 cm. Dotted lines represent the transmitter coils used for the simulation. **c,** Coupling coefficient between the soft transmitter and implanted receiver coils with varied lateral (red) and vertical (naval) distances. **d,** Coupling coefficient between the soft PSPN (red) or rigid (naval) transmitter coil and the implanted receiver coil with varied phantom radii (h=1 cm). **e**, Transfer efficiency of the WPT system comprising the stretchable PSPN transmitter and implanted receiver, as a function of tensile strain. Extracted efficiency at 50 MHz appear in the inset, indicating the strain-insensitive performance for up to 50% strain. Here, the phantom radius is 5.5 cm, and the implantation depth is 1 cm. **f**, Photographs of a stretchable wireless powering system. A stretchable transmitter coil made of PSPN was used to power a red LED device implanted in fish, demonstrating robust and reliable operation when stretched at 50% strain. Scale bars, 2 cm. **g**, Quantitative brightness of the LED wirelessly powered by the transmitter made of the PSPN and conventional Ag NWs under strain. **h**, Schematic illustration of the *in vivo* demonstration for the implantable wireless power transfer system. An implantable optoelectronic device is subcutaneously implanted between the skin and muscle on the ventral side of the animal. The transmitter wirelessly delivers RF power to the implanted

optoelectronic device with precise control over its operation, while allowing for unrestricted movement of the animal. **i**, Photograph of an implanted mouse freely behaving in an NFC-powered setup. Scale bar, 2 cm.

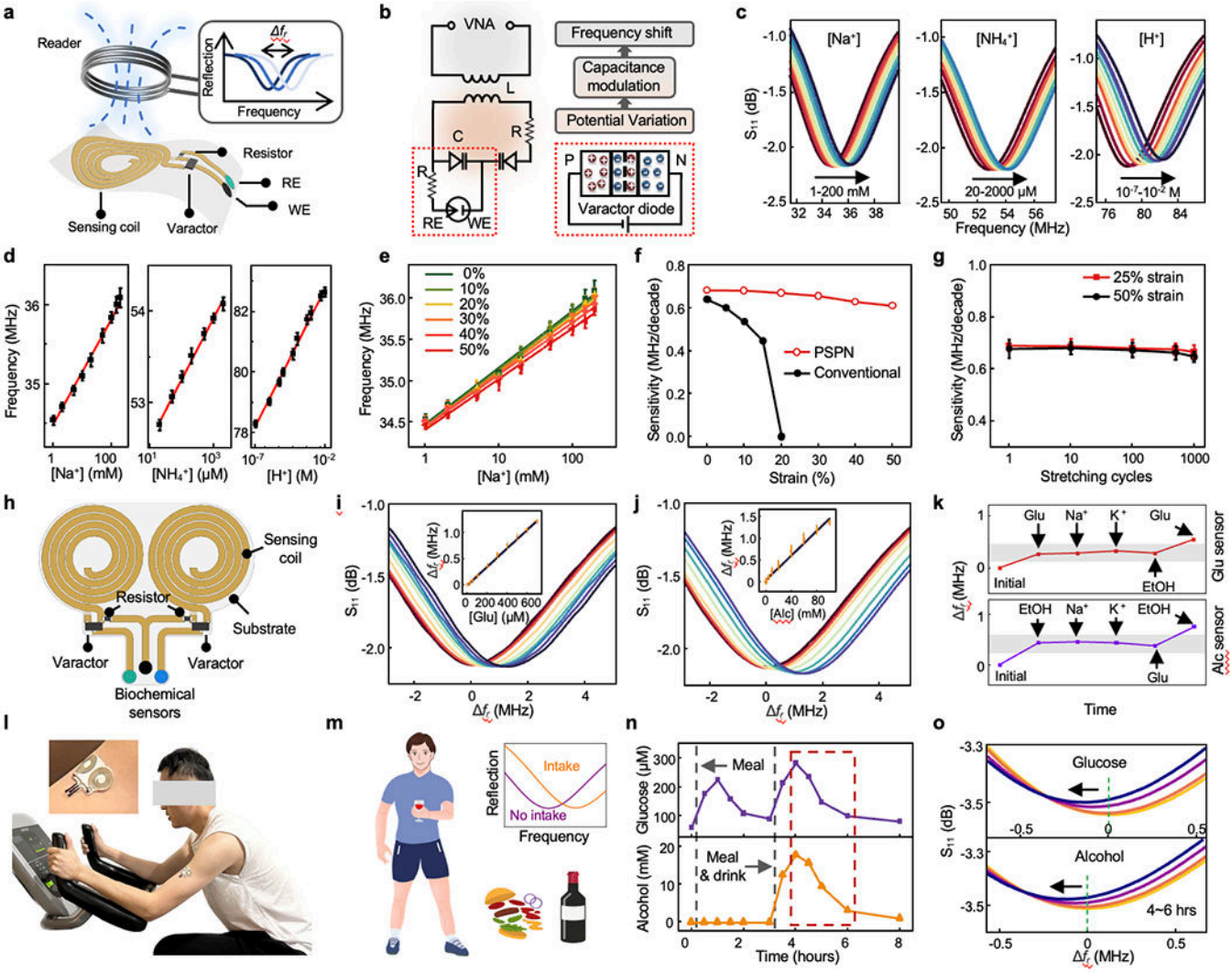

Fig. 5. Wireless stretchable bioelectronics for multiplexed biochemical sensing.

a, Schematic illustration of the stretchable, battery-free, and wireless *LC* circuit–based bioelectronics for biochemical sensing. RE, reference electrode; WE, working electrode. **b**, Equivalent circuit, and operation principle of the wireless sensing system. **c**, **d**, Reflection coefficients (**c**) and frequency shifts (**d**) for wireless Na^+ (1–200 mM), NH_4^+ (20–2000 μM), and H^+ (10^{-7}–10^{-2} M) monitoring. **e**, **f**, Frequency shifts (**e**) and sensitivity (**f**) of the wireless Na^+ sensing system made of PSPN (red circle) and conventional Ag NWs (black solid) under strain. **g**, Alterations in sensitivity observed in the Na^+ sensing system after subjecting the PSPN device to 1,000 repetitive stretching cycles at strain levels of 25% and 50%. **h**, Schematic of wireless on-body stretchable bioelectronics for multiplexed biochemical sensing. **i**, **j**, Reflection coefficients for wireless on-body glucose (**i**) and alcohol (**j**) monitoring. Calibration plots appear in the inset. **k**, Selectivity tests of the multiplexed sensing system. Glucose (top) and alcohol (bottom) sensor responses to the addition of target molecules and interfering biomarkers, including glucose (150 μM), Na^+ (20 mM), K^+ (5 mM), ethanol (20 mM). **l**, Photograph of a volunteer wearing a multiplexed wireless biochemical sensing system during cycling exercise. **m-o**, Illustration (**m**) and dynamic

wireless analysis of sweat glucose and ethanol levels (**n**, **o**) with and without intake of food and drink over a course of 8 hours. Sweat secretion was triggered by a 10-min session of constant-load stationary cycling. Raw data from 4 to 6 hours in (**n**) is depicted in (**o**). Error bars in (**d**), (**e**), (**g**), (**i**) and (**j**) represent standard deviations of the mean from three samples.